Hydrodynamic Effects in Low-Grazing Angle Backscattering from the Ocean

Enrique A. Caponi, Bruce M. Lake, and Henry C. Yuen

***Abstract*— Time series of returned power, Doppler spectra and range versus time intensity (RTI) images collected from low-grazing angle radar backscattering from the ocean present features which cannot be explained solely within the framework of resonant Bragg scattering. We propose that most of the observed characteristics are a consequence of the way in which waves evolve on the surface of the ocean. To illustrate this point, we have built a model consisting of a hydrodynamic module and a radar response module. The hydrodynamics module includes most of the physics thought to be relevant to the evolution of a wavefield (i.e., nonlinear interactions, wind, and wavebreaking). The radar module computes the backscattering as the accumulation of Bragg response from every tilted facet of the reconstructed surface, except for those locations where hydrodynamic conditions leading to wavebreaking are detected. Facets involved in wavebreaking are assumed to contribute to the backscattering in a quasi-specular polarization independent fashion. The hydrodynamics module is used to simulate the evolution of a nonlinear wave field, starting from essentially monochromatic conditions. The evolution reproduces known characteristics of these systems, including the generation of sideband instabilities and downshifting. The radar response module is then exercised on the resulting surface at various stages of development. Simulated RTI's at very low-grazing angles reproduce the observed polarimetric characteristics, as well as their behavior when the grazing angle is increased. Simulated Doppler spectra reproduce the peak separation phenomenon observed in field measurements at very low-grazing angles and also show a behavior similar to that shown by field data when the grazing angle is increased.**

***Index Terms*—Hydrodynamic effects, scattering, sea.**

I. Introduction

RECENT low-grazing angle radar backscattering measurements from the ocean (Ward *et al.* [30], Lee *et al.* [12], [13], [17]) have established that the observed microwave returns can not be explained solely within the framework of resonant Bragg scattering (e.g., Rice [25]; Valenzuela [28]). Striking features of the field data at these angles are the appearance of bursts or spikes—much more apparent at horizontal (HH) polarization than at vertical (VV)—in time series of the returned power, the appearance of "stripes" in range versus time intensity (RTI) images and the occurrence of "fast" peaks in time averaged Doppler spectra. Furthermore, the overall ratio of HH to VV polarized return power does not approach zero with grazing angle, as predicted by Rice's theory. Some of these characteristics had been observed in earlier field experiments and had been associated with breaking waves (e.g., Kalmykov and Pustovoytenko [8], Wetzel [32]; Jessup *et al.* [7]).

In fact, a series of very careful laboratory experiments (Lee *et al*. [14]–[16], [18]–[22]) show similar characteristics for the radar backscattering from mechanically generated waves at various levels of breaking. These results strongly indicate that several different scattering mechanisms have to be taken into consideration. It is expected that from the analysis of these detailed, high-resolution measurements, the dominant mechanisms responsible for the observed behavior will be identified and quantified, so that physically meaningful parameterizations can be incorporated in the simulation of at-sea returns.

Here, a model is proposed to show that regardless of the actual physical mechanisms responsible for the microwave scattering, significant features observed in field data can be reproduced by postulating that non-Bragg scatterers are generated by breaking waves or waves in incipient stages of breaking. In order to do this, we simulate the evolution of a nonlinear wave field in time under the effect of wind, identifying at every step in the evolution the regions where wave breaking is likely to occur. Microwave backscatter is calculated under the assumption that the reconstructed surface is populated by Bragg scatterers consistent with the applied wind, except in facets involved in wave-breaking, where a population of scatterers is assumed advected by the wave crest. For the purposes of this illustration, these non-Bragg scatterers are specified to respond quasi-specularly for the incidence angles of interest.

This very simple radar backscattering model, when applied to surfaces generated by a code that captures most of the dynamics known to be relevant in the evolution of ocean waves, yields simulated results that show very good qualitative agreement with observations and with trends in the experimental data as a function of grazing angle.

II. Hydrodynamic Model

In the open ocean, unsteadiness induced by both wind input and nonlinear interactions facilitate the deformation and eventual breaking of surface waves at average steepness values well below those determined theoretically to be the maximum values for steady waves. As a consequence, microbreaking (i.e., the process of tipping over of the crest of the wave, as opposed to the more violent, and not so frequent, activities leading to whitecapping) is fairly abundant in the ocean, even under light to moderate wind conditions.

Manuscript received February 2, 1998; revised July 17, 1998. This work was supported by the Advanced Sensors Applications Program in the Intelligence Systems Support Office, Department of Defense, under Contract DMA 800-94-C-6008.

The authors are with TRW Space and Electronics, Redondo Beach, CA 90278 USA.

Publisher Item Identifier S 0018-926X(99)03720-5.

To describe most of the physics responsible for these properties, we simulate the long term evolution of a wavefield taking into account the modulation of nonlinear surface waves (Yuen and Lake [33]), the effect of dissipation due to (micro)breaking, and the interaction between the evolving wavefield and the existing wind. The description is based on the formulation introduced by Zakharov [34] for a broad-band spectrum of waves. The time evolution of spectral components in a weakly nonlinear dispersive wave system in which four-wave interactions dominate in the time scale of interested is governed by

$$dD_1/dt + i\Omega_1 D_1 = -i \sum_{0<k_2,k_3,k_4\le k_{\max}} K_{1234} D_2^* D_3 D_4 \delta(k_1+k_2-k_3-k_4). \quad (1)$$

In (1), $D_i = D(k_i,t)$ are complex variables combining the Fourier transforms of the slow time components of the water surface displacement $\eta(x,t)$ and of the surface velocity potential $\varphi(x,\eta(x,t),t)$, via $D(k_i,t) = \hat{\eta}(k_i,t) + i(k_i/g)^{1/2}\hat{\varphi}(k_i,t)$.

In (1), the interaction coefficients K_{ijkl} are real functions of the wavenumber arguments first derived by Zakharov [34] and shown, with some minor corrections, in Crawford *et al.* [4]. However, in that early version, the resulting reduced equations (1) are not Hamiltonian, as observed by various authors (e.g., Caponi *et al*. [2]. The version used here is due to Krasitskii [9], [10], who determined the reason for this defect and removed it by formally applying the classical method of canonical transformations in the determination of the interaction coefficients.

The quantity Ω is determined by the deep water dispersion relation for gravity waves, and by the generation and dissipation processes that we choose to include in the model. In the absence of these latter processes, its value coincides with $\omega(k_i) = (gk_i)^{1/2}$, where k_i is the wavenumber and $g = 9.81$ m/s^2 is the gravitational acceleration.

Wave growth due to wind is modeled as in Snyder *et al.* [27]. The linear growth rate β—a function of wavenumber k and wind speed at the reference height—is incorporated as the imaginary component of Ω in (1). The evolving wavefield is allowed to modify the applied wind profile via a simplified formulation that follows Janssen *et al.* [6], requiring that the wind speed on a nonuniform mesh set in the air be solved at every time step.

Zakharov's equation describes accurately the behavior of the wave envelope, but does not describe the detailed properties of a breaking wave. Here, these properties are parameterized via a wave-breaking model that accounts for the energy loss due to this process.

Dissipation is taken to be molecular, except when breaking conditions at the surface are present. Breaking is assumed to occur when the maximum value of the local slope exceeds a pre-established steepness $ka_{\rm cap}$. Following Lake *et al.* [11], we model this dissipation as

$$\nu_{wvb} = \nu_1 \exp\{\mu((ka - ka_{\rm cap})/(ka_{\lim} - ka))\} \quad (2)$$

where ka is the maximum slope in the reconstructed surface, $ka_{\rm cap}$ is the steepness beyond which incipient breaking is assumed to occur, and $ka_{\lim}$ is the maximum physically attainable steepness. The values taken for the adjustable parameters are $\nu_1 = \nu_m$ (molecular viscosity) and $\mu = 1$.

Hence, the final expression for Ω used in (1) is

$$\Omega_i = \Omega(k_i) = \omega_i + i\big(\beta(k_i, U_{10}) - \nu_T k_i^2\big) \quad (3)$$

where ν_T is either the value for ν_{wvb} of (2) or the molecular viscosity ν_m, depending on whether the maximum local slope exceeds $ka_{\rm cap}$ or not.

Since the criterion for wave breaking used above is dependent on the local steepness values, the surface has to be reconstructed at every time step. For the purposes of the simulations presented here, the first-order accurate expression for the slow-time surface displacement

$$\eta(x,t) = \left(\sum_i D(k_i,t)\exp(ik_i x) + \text{c.c.}\right) \Big/ 2\pi \quad (4)$$

is used throughout. Results are slightly different when using the improved linear representation (ILR) of Creamer *et al.* [5], but this happens at a substantial cost in running time without changing the nature of the conclusions reached here.

III. Wavefield Evolution

In the one-dimensional (1-D) code implementing this model, the wavesystem is described by a mesh of N modes, uniformly distributed in k space. For the simulations described here, N was chosen to be 31, resolving waves between about 40 cm and 4π m. This choice of k values permits the description of a reasonable portion of the gravity wave spectrum for a young sea, while the chosen value of N allows for fast execution times with modest computational hardware. Initial conditions consisted of an essentially monochromatic wavefield, with a wavelength of 78.5 cm and an initial slope $ka = 0.10$. The amplitude of the other 30 modes was set to a relative level of 10^{-4}, and their phases chosen randomly. A range of values could be reasonably chosen for the parameters of the wavebreaking model. Here, we used the typical values $ka_{\rm cap} = 0.2$ and $ka_{\lim} = 0.3$. Details of the wavefield evolution, as well as global indicators (temporal evolution of the wavefield energy, frequency of breaking events, etc.) are dependent on the values chosen for these characteristic slopes, but those variations are not relevant to our purposes here. The initial wind profile was taken as logarithmic, with an initial strength of 10 m/s at the reference height of 10 m, and was described by a nonuniform mesh of 15 points, extending to a height of 150 m above the mean surface level, i.e., several times the wavelength of the longest water wave described.

The wavefield development is described by Figs. 1–3. In the top panel of Fig. 1, the total energy of the wave system is displayed as a function of time. The ragged trace is composed of a series of nearly exponential growth periods due to wind input, interspersed with abrupt jumps corresponding to the dissipative character of wavebreaking events. Due to the change in time of the wave spectrum, the growth rate values during calm periods between breaks vary as a function of time. The overall "effective" growth rate of the wavesystem is smaller—by a factor of almost five—than the initial growth rate.

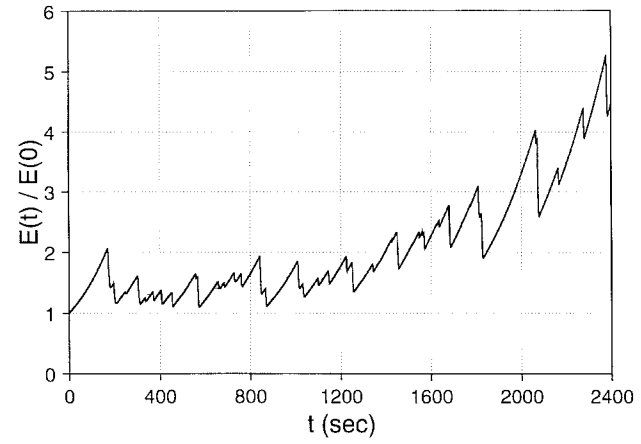

(a)

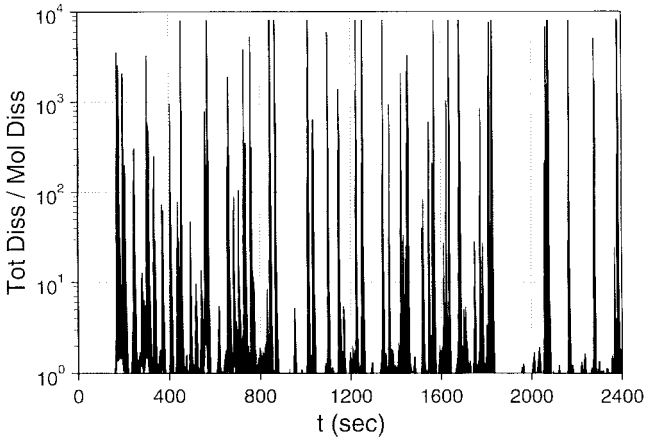

(b)

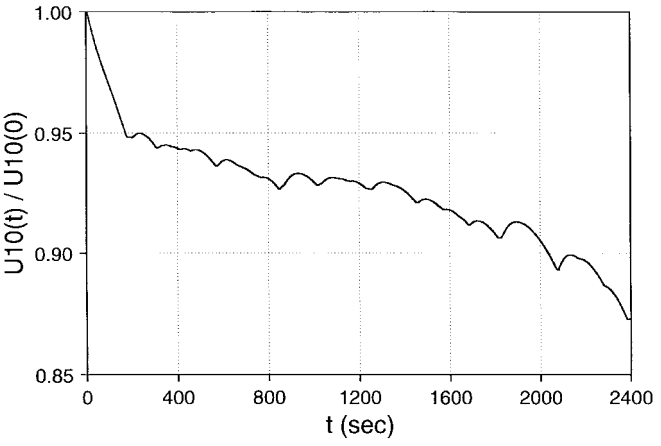

(c)

Fig. 1. Evolution of the wind-wave system described in the text. (a) Total energy in the wave system. (b) Total dissipation referred to the molecular dissipation. (c) Wind speed at reference height referred to its initial value.

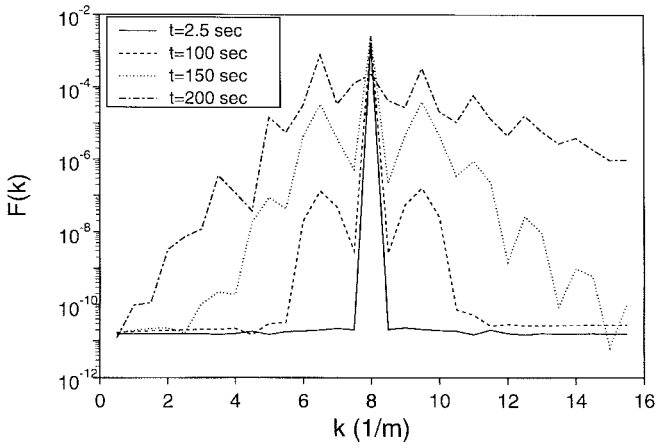

(a)

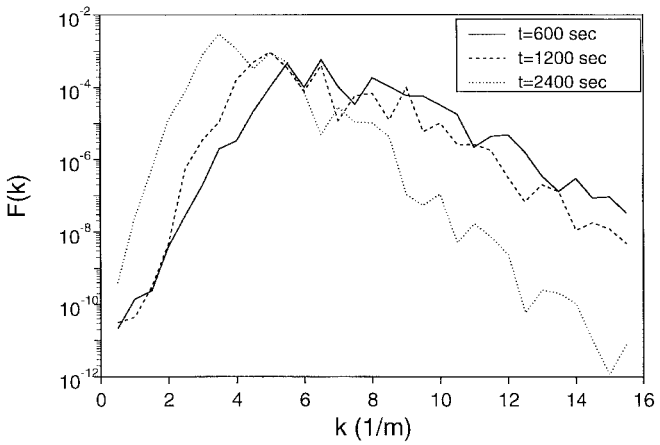

(b)

Fig. 2. Wave spectra at various times averaged over 3 s for the system of Fig. 1. First wavebreaking event occurs at approximately 160 s.

The time evolution of the total dissipation in terms of the molecular dissipation is displayed in the middle panel of Fig. 1. As expected, the largest peaks in this quantity align with the energy loss events shown in the top panel. The bottom panel shows the time evolution of the applied wind U_{10} at the reference height.

Traces of the wave spectrum at selected times are shown in Fig. 2. Note the initial appearance of side bands and the roughly symmetrical character of the spectrum for traces corresponding to times earlier than the first wavebreaking event (at about 160 s). For later times, the spectrum is clearly asymmetric showing that the wave system undergoes downshifting. This phenomenon is shown more clearly in Fig. 3 where spectrum levels are color coded and displayed in k-t space. These results reproduce observed characteristics in the evolution of water waves: excitation of Benjamin–Feir instability in a nonlinear wavetrain and, in the presence of breaking, downshift in the wave spectrum (Lake *et al.*, [11]).

IV. Simulation of Radar Return

We assume that a beam of parallel rays at the specified grazing angle shines on a full period of the reconstructed surface, and that surface facets in the geometric shadow do not contribute to the return.

Illuminated facets are assumed populated by a spectrum of short waves consistent with the applicable value of the wind speed at the reference height, via either Pierson–Stacy's [24] spectrum, or the Donelan–Banner–Jähne spectrum due to Apel [1]. For each of these facets, the local grazing angle $\theta_{\rm gi}$ as a function of the nominal grazing angle θ_g and the local long-wave surface slope is calculated, thus determining the local

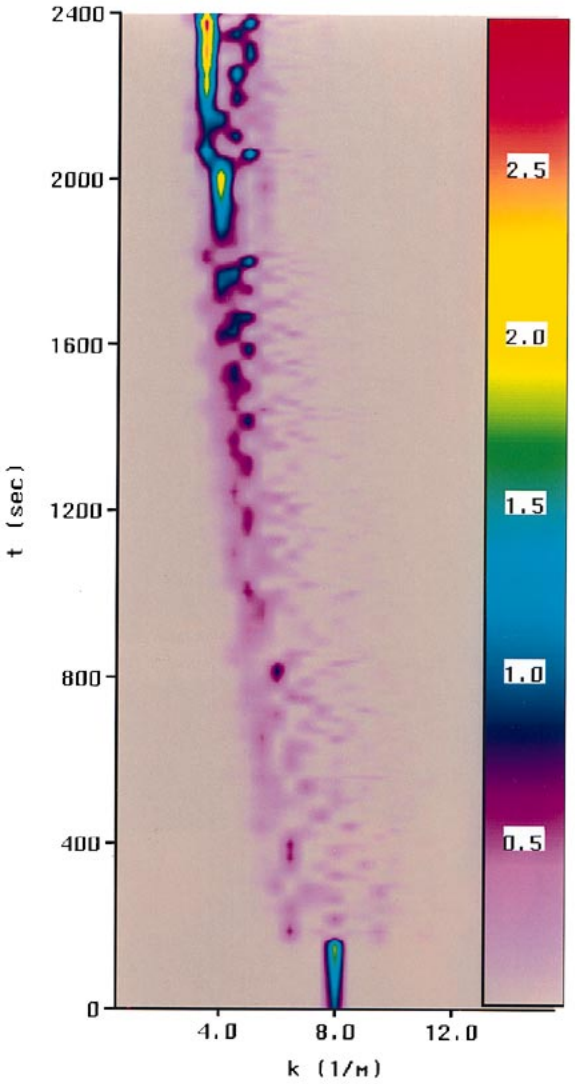

Fig. 3. Normalized wave spectrum $F(k,t)/F(k_0,t=0)$. Horizontal axis is wavenumber k, extending between 0.5 and 15.5 m^{-1}. Vertical axis is time extending from 0 to 2400 s.

resonant Bragg wavenumber $k_B = 2k_r \cos\theta_{\mathrm{gi}}$, where k_r is the radar wavenumber. For illuminated facets not involved in wavebreaking, the backscatter power is calculated using Valenzuela's [29] expressions for the normalized cross sections per unit area σ_{HH} and σ_{VV}, evaluated at the local resonant wavenumber, for a dielectric value $(\varepsilon = 51.4 - i39.1)$ corresponding to the environment considered in Lee *et al.* [12].

Facets involved in wavebreaking are assumed to return—per unit area—a large fraction of the incoming power along the direction of incidence, regardless of the incoming polarization and grazing angle (within the range of grazing angles of interest.) Due to the limitation imposed by the use of a 1-D scattering surface, the value used for the corresponding cross section per unit area depends on the illumination pattern of the instrument whose response is being simulated. The 1-D surface is well suited for the case of a scatterometer whose footprint on the ocean surface is of the order of a few meters in the radial direction and sufficiently narrow in the azimuthal direction so that variations in the scattering surface in this direction can be safely ignored. On the other hand, for characteristic beamwidths and ranges used in ocean probing, a range-gated radar typically covers an azimuthal width of the order of tens of meters and azimuthal variations in the surface wave field must be accounted for. For a given range gate, the strength of the contribution from scatterers generated by a breaking event, whose azimuthal extent is expected to be substantially smaller than the illuminated azimuthal width, will be diluted by the Bragg contribution from the majority of the illuminated region at the range gate of interest. Consequently, the effective non-Bragg cross section per unit area to be used in the simulation of the response to this type of instrument should be substantially smaller than the value used in the simulation of a narrow spot size radar.

The heuristically determined values used in the generation of the results presented below for the effective non-Bragg cross section per unit area σ_{nB} are 0.3 for an instrument illuminating a small azimuthal extent and 0.05 for a typical range-gated radar at a mean range of the order of a few kilometers. These values are consistent with the recently determined value for the non-Bragg HH cross section obtained in high-resolution laboratory measurements on breaking waves (Lee *et al.* [22]) and with their estimate for the effective value on ocean data collected with a range-gated radar.

Simulated range-time intensity (RTI) plots are built collecting the response for each polarization from each surface facet at the range bin corresponding to the facet's position. Since RTI's are a product of range-gated radars, the value $\sigma_{\mathrm{nB}} = 0.05$ is used in their simulation.

In order to simulate a time-averaged Doppler spectrum, the returned power from each facet is accumulated on the frequency bin containing the Doppler frequency f_D that corresponds to the projection along the radar wavevector $\mathbf{k}_r$ of the speed $\mathbf{u}_s$ at which the scatterer type responsible for the return propagates: $2\pi f_D = -2\mathbf{k}_r \cdot \mathbf{u}_s$.

For Bragg contributions, $\mathbf{u}_s$ is the phase speed of the resonant Bragg waves, added to the local orbital velocity due to the long wave field and the wind induced drift velocity. For the non-Bragg contributions, the relevant speed is the local phase speed of the breaking facet, obtained as the ratio of the local wave frequency to the local wavenumber, both determined via the Hilbert transform of the reconstructed long wave surface (Melville [23]) added to the drift velocity.

In addition, broadening mechanisms affecting the calculated Doppler return for both types of contributions (and irrelevant in the simulation of RTI's) have been incorporated in the code. These are summarized below; details can be found in Caponi [3].

The width of the Bragg peak in the Doppler spectrum is mainly determined by the distribution of orbital velocities of the long wave field on which the Bragg scatterers propagate (the broadening produced by variations in the effective incidence angle over the scattering region in the case of radars close to the illuminated surface being ignored at this stage.) The hardware used to exercise this code forces the range of wavenumbers described to be rather limited when compared with at-sea experiments. As a consequence, the broadening of the Bragg peaks in the simulated Doppler spectra is not as

large as that characteristically found in the open ocean data. We model the effect of longer waves not described by the k-mesh by adding to the Doppler frequency for each Bragg contribution a normally distributed deviate with zero mean and a variance chosen to be consistent with representative spectra obtained from field data. We have taken the value $B_w = 19$ Hz as representative for the $1/e$ Gaussian half-width of the Bragg contribution.

Non-Bragg contributions to time averaged Doppler spectra have been found to follow a Lorentzian—in general, a Voigtian—distribution (Lee *et al.* [12], [13]). This behavior is consistent with the interpretation that these contributions are due to scatterers with a finite lifetime, where the corresponding frequency can be determined with an uncertainty inversely proportional to the event's lifetime. In this implementation, we assume that each "breaking facet" contains a large number of scatterers $(N = 100)$, each of which returns $1/N$ of the power assumed to be returned by a facet involved in wavebreaking by the value of σ_{nB} in use. These N contributions are assigned to the Doppler frequency bin corresponding to the local phase speed, each shifted by a Lorentzian distributed deviate with zero mean and a half-width of 10 Hz. Doppler spectra shown in the next section are obtained by averaging instantaneous spectra collected over the specified time intervals.

The electromagnetic scattering model described above is known to be incomplete. Both field measurements (Lee *et al.* [17]) and detailed probing of breaking waves in the laboratory (Lee *et al.* [16], [18], [22]) show that single-bounce specular-like events like the ones modeled here exist, but may not be the predominant mechanism generating non-Bragg contributions. The experimental results show that the HH/VV ratio for non-Bragg events is not one as assumed here (it is not even constant over the various stages of development of a breaking wave) and that time series of cross-pol returns HV and VH over a breaking event differ. Other mechanisms (e.g., Brewster reflection in double bounce scattering, scattering from three dimensional surface features, large curvature effects, etc.) must be invoked to account for these observations.

However inaccurate our modeling of non-Bragg scattering may be, its use is not critical to the objective pursued, which is to show the relevance of nonlinear wave dynamics in the explanation of some of the most striking characteristics of radar return at low-grazing angles.

V. Results

The model described above was used to obtain simulated radar response outputs at particular stages of evolution of the wave field. Of interest are the range versus time intensity plots and Doppler spectra.

A. Simulated RTI's

Simulated RTI's for VV and HH polarization at various grazing angles are shown in Fig. 4, corresponding to the wavefield generated between $t = 1000$ and $t = 1030$ s. In each panel, radar range increases from right to left (the width being 4π m) and time increases upwards (from 0 to 30 s). Intensities are mapped linearly to a monochromatic scale from black to white over 256 levels.

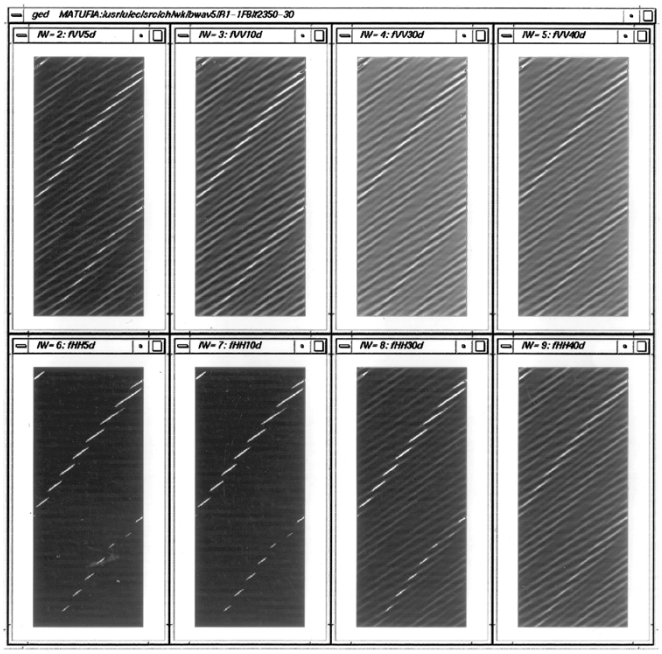

Fig. 4. Simulated RTI's for 5°, 10°, 30°, and 40° grazing for a 30 s interval starting at $t = 1000$ sec. Top row: VV polarization. Bottom row: HH polarization. Range increases to the left from 0 to 4π m. Time increases upwards from 0 to 30 sec.

Qualitatively similar RTI's for both polarizations are produced at large grazing angles (rightmost column in Fig. 4, corresponding to 40° grazing). For lower grazing angles, the respective images become quite different.

As the grazing angle is reduced, the character of the VV response does not change significantly. While shading, manifested by the dark (no return) bands, becomes more apparent as the grazing angle is decreased, the wave system can still be recognized for this polarization even at 5° grazing.

For the HH case, on the other hand, as the grazing angle is decreased the non-Bragg contributions become dominant, and the imaging of the wave system is lost. What remains at very low-grazing angles is a collection of short stripes identifying the location of the wavebreaking events in the range-time plane. The slope of the stripes is the phase speed of the breaking waves, the stripes being organized in bands whose slope is the corresponding group speed.

Similar characteristics are apparent in RTI's collected in the open sea (cf., for example, Ward *et al.* [30], Ward and Shepherd, [31], and Smith *et al.* [26]).

B. Simulated Doppler Spectra

Figs. 5–7 reproduce 2-min averaged ocean data Doppler spectra at various grazing angles published by Lee *et al.* [12]. In each case, the VV and HH instrument response is shown as thick solid and dashed lines, respectively, while the corresponding simulated response is displayed as thin lines of the same type.

The Doppler spectra of Fig. 5 correspond to data obtained by the Royal Signals and Radar Establishment (RSRE) in Loch Linnhe, Scotland, 1989. The instrument was a range gated X-band radar operating at 10 GHz, mounted on the

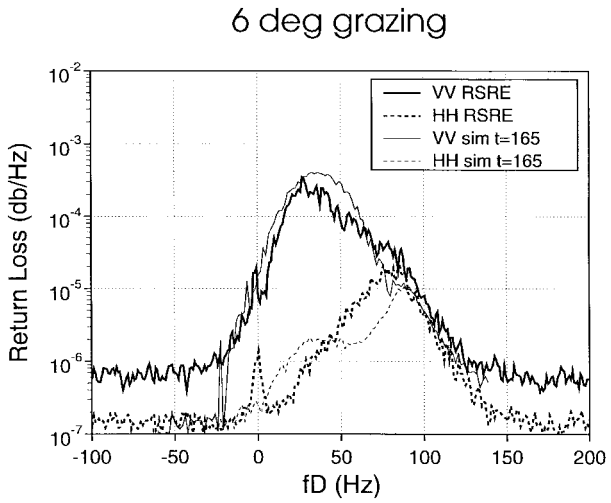

Fig. 5. Doppler spectra at 6° grazing. Experimental data (thick lines) from Loch Linnhe Experiment, 1989, Run 8, range cell 80, obtained by Royal Signals and Radar Establishment (RSRE). Simulated spectra collected over a 5 s interval starting at $t = 165$ s are displayed with thin lines. In both cases, solid lines are used for the VV response, dashed lines for HH.

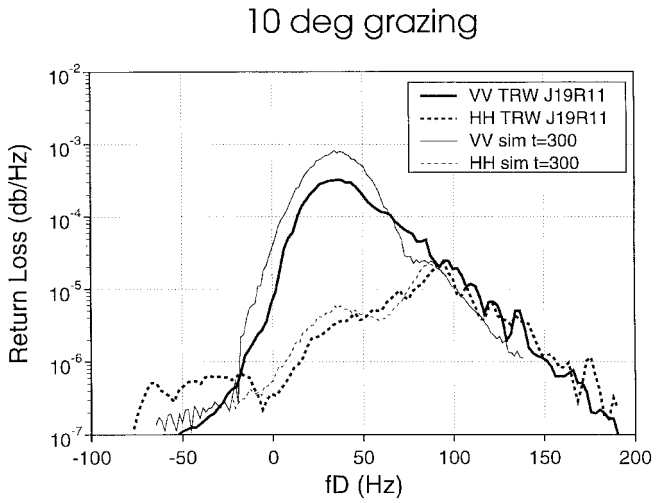

Fig. 6. Doppler spectra at 10° grazing. Experimental data (thick lines) obtained by TRW's scatterometer in Sound of Sleat, Scotland, 1991, has been shifted in frequency to remove the boat's speed contribution to the Doppler shift. Simulated spectra collected over a 10 s interval starting at $t = 300$ s are displayed with thin lines. In both cases, solid lines are used for the VV response, dashed lines for HH.

coast at a nominal range of 2.5 km, with a range resolution of 1.5 m and a nominal azimuthal coverage of 43 m. The data displayed corresponds to range cell 80 and the corresponding grazing angle is about 6°. The wind speed was about 8 m/s, and the look angle was about 60° with respect to the wind direction (which makes this case not a very good candidate to be simulated by the 1-D model described here).

The spectra of Figs. 6 and 7 were obtained by TRW in Sound of Sleat, Scotland in 1991. The instrument was a CW dual-polarization X-band (9.2 GHz), coherent scatterometer mounted on the bow of a boat at about 2.3 m over the mean water surface. The data were collected at nominal grazing angles of 10° and 25°, respectively. In both cases, the boat (and, consequently, the radar) was aligned against the wind, which was determined to be 8.5 m/s and 9.5 m/s at 10 m height, respectively. The boat speed was about 1.1 m/s for both cases.

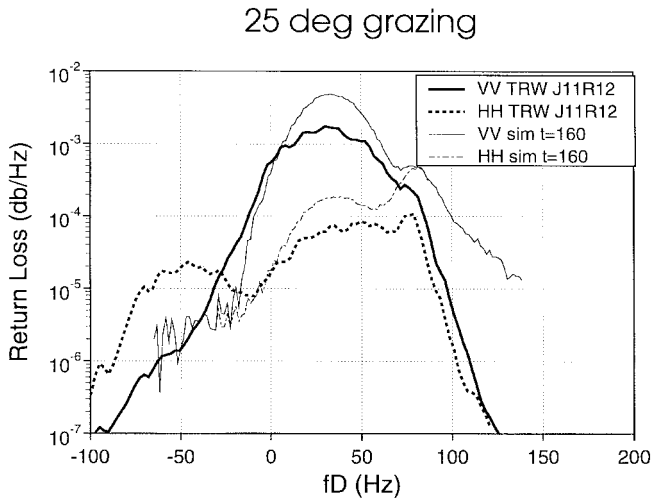

Fig. 7. Doppler spectra at 25° grazing. Experimental data (thick lines) obtained by TRW's scatterometer in Sound of Sleat, Scotland, 1991, has been shifted in frequency to remove the boat's speed contribution to the Doppler shift. Simulated spectra collected over a 10 s interval starting at $t = 160$ are displayed with thin lines. In both cases, solid lines are used for the VV response, dashed lines for HH.

The data has been shifted in frequency to compensate for the Doppler shift due to the boat's speed.

In each of these figures, thin lines display 10 s averaged simulated spectra for the corresponding grazing angle. The starting times have been chosen so that the peak in the response due to the non-Bragg contributions (the "fast" peak) occurs at approximately the same Doppler frequency as the corresponding feature in the experimental data.

For the 6° grazing simulation, the effective normalized cross section for non-Bragg response was taken as $\sigma_{\mathrm{nB}} = 0.05$, given that the experimental data was collected over a strip extending approximately 43 m in the azimuthal direction. The 25° grazing angle data is the response to an instrument illuminating a very small footprint, whose major (radial) and minor (azimuthal) semi-axes were about 1.2 m and 0.5 m. For this case, the value $\sigma_{\mathrm{nB}} = 0.3$ was used.

The appropriate value for σ_{nB} to use in the 10° case is more difficult to determine. Although the nominal azimuthal semi-axis is of the order of 1.5 m, the calibration found the instrument's vertical plane −3-db beamwidths to be 8.7° for VV and 10.3° for HH, thus rendering the radial extent of the illuminated footprints very large at this grazing angle. A further uncertainty is introduced by the observation that maximum instrument platform pitch was estimated to be of the order of 1.25° for this series of experiments. Consequently, it has been assumed that for this grazing angle the illuminated footprint in the experiment was substantially larger than the illuminated footprint in the simulation and the value $\sigma_{\mathrm{nB}} = 0.05$ was adopted.

The traces corresponding to data and to simulated responses in Figs. 5 to 7 share several distinctive traits. In all sets, the HH spectrum peaks at a Doppler frequency larger than the Bragg frequency at which the VV spectrum peaks, while a secondary HH peak at the Bragg frequency becomes more prominent as the grazing angle is increased. The VV spectrum profile is asymmetric due to the non-Bragg contributions.

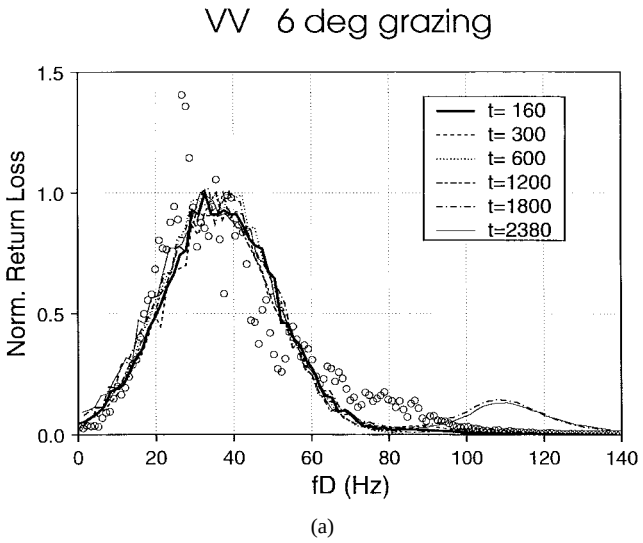

Fig. 8. Simulated normalized Doppler spectra at 6° grazing collected over 10 sec intervals at various stages of development of the simulated wavefield evolution. The case starting at $t = 600$ s contains a single wavebreaking event, while the others contain a series of events. The experimental data described in Fig. 5 is plotted as open circles. (a) VV response normalized with respect to its maximum. (b) HH response normalized with respect to its value at the "fast" peak.

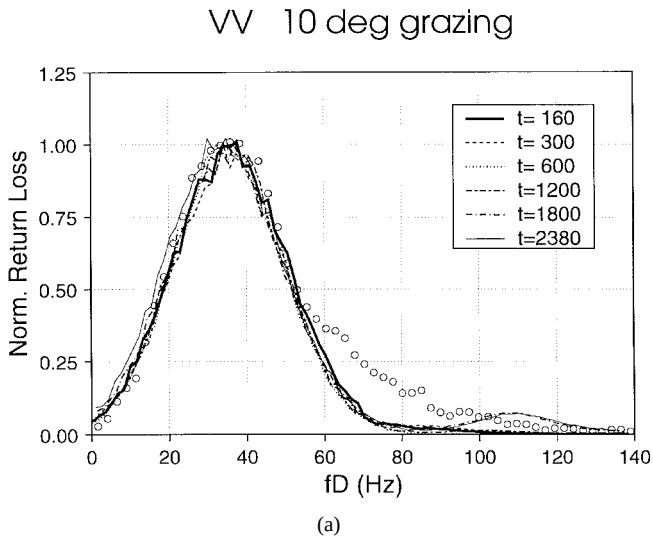

Fig. 9. Simulated normalized Doppler spectra at 10° grazing. The experimental data described in Fig. 6 is plotted as open circles (see Fig. 8 caption).

In the 6° grazing case shown in Fig. 5, the complete peak separation between VV and HH observed in the data is almost reproduced, were it not for a minor peak in HH close to the Bragg frequency. This is not surprising, given that the simulation assumes a population of Bragg waves corresponding to a wind speed of about 9.5 m/s at 0° look angle, while the experimental conditions correspond to a head wind component of about 4 m/s. However, as the wave field evolves, complete peak separation is obtained in the simulated results also [cf. Fig. 8(b)].

Normalized simulated and 10 s averaged, Doppler spectra at various stages of development of the wavefield are superposed to the experimental data (averaged over approximately 2 min) in Figs. 8–10, for the grazing angle cases 6°, 10° and 25°, respectively. VV spectra are normalized with respect to their maximum value, while HH spectra are normalized with respect to the maximum value at the fast peak. With the exception of the collection starting at $t = 600$ s (where only one wavebreaking event occurs), all collection periods are characterized by active wavebreaking. The main contribution to the simulated VV response does not change appreciably with the wavefield, but the extent and level of the long tail for frequencies larger than the Bragg frequency does. The simulated normalized HH response at different times in the (b) panels of Figs. 8–10 show a predominantly "fast" response whose Doppler frequency increases in time as the dominant wave becomes longer and a smaller contribution at the Bragg Doppler frequency whose value relative to the "fast" peak depends on the stage of development of the wavefield and the frequency of wavebreaking events. Note that the Bragg peak can become dominant when wave breaking activity is low in the collection interval (see trace corresponding to $t = 600$ s).

The measured and simulated normalized HH Doppler spectra as a function of the normalized (with respect to the frequency of the "fast" peak) Doppler frequency are displayed in Fig. 11, one panel for each of the grazing angles under consideration. As the grazing angle is increased, the data shows the Bragg contribution increasing, a trend

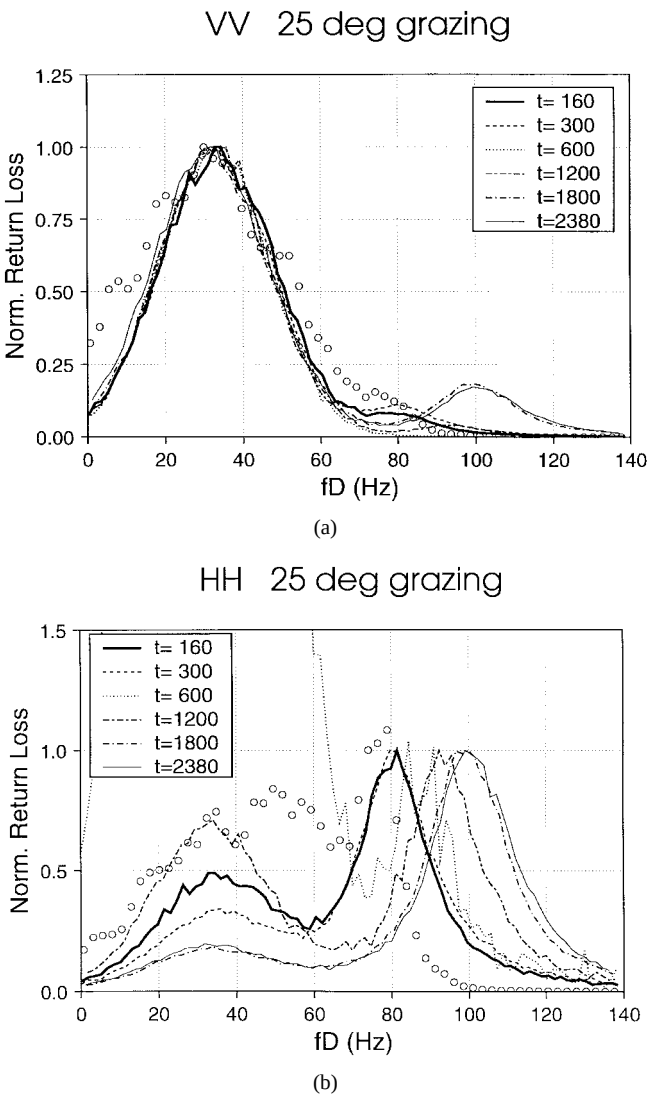

Fig. 10. Simulated normalized Doppler spectra at 25° grazing. The experimental data described in Fig. 7 is plotted as open circles (see Fig. 8 caption).

reproduced by the simulated results. Shortcomings in the simple electromagnetic model used (for example, neglecting the effect on the microwave return of features appearing just behind a breaking wave and their subsequent adjustment to the predominant flow) seem to become more apparent as the grazing angle increases [compare Fig. 11(c) to Fig. 11(a) and (b)]. In all cases, most of the data falls within the envelope defined by the simulated results.

VI. Conclusion

A very simple backscatter model applied to an evolving ocean surface generated by a dynamical model incorporating the relevant hydrodynamics (nonlinear interactions, wind and wavebreaking) has been shown to produce simulated radar returns that capture characteristics that make low-grazing angle radar returns from the open ocean inconsistent with a Bragg-only interpretation. The simulated range-time intensity plots at very low-grazing angles reproduce the observed polarimetric characteristics: relatively smooth power variations in VV, very large variations in HH, usually arranged in bands which

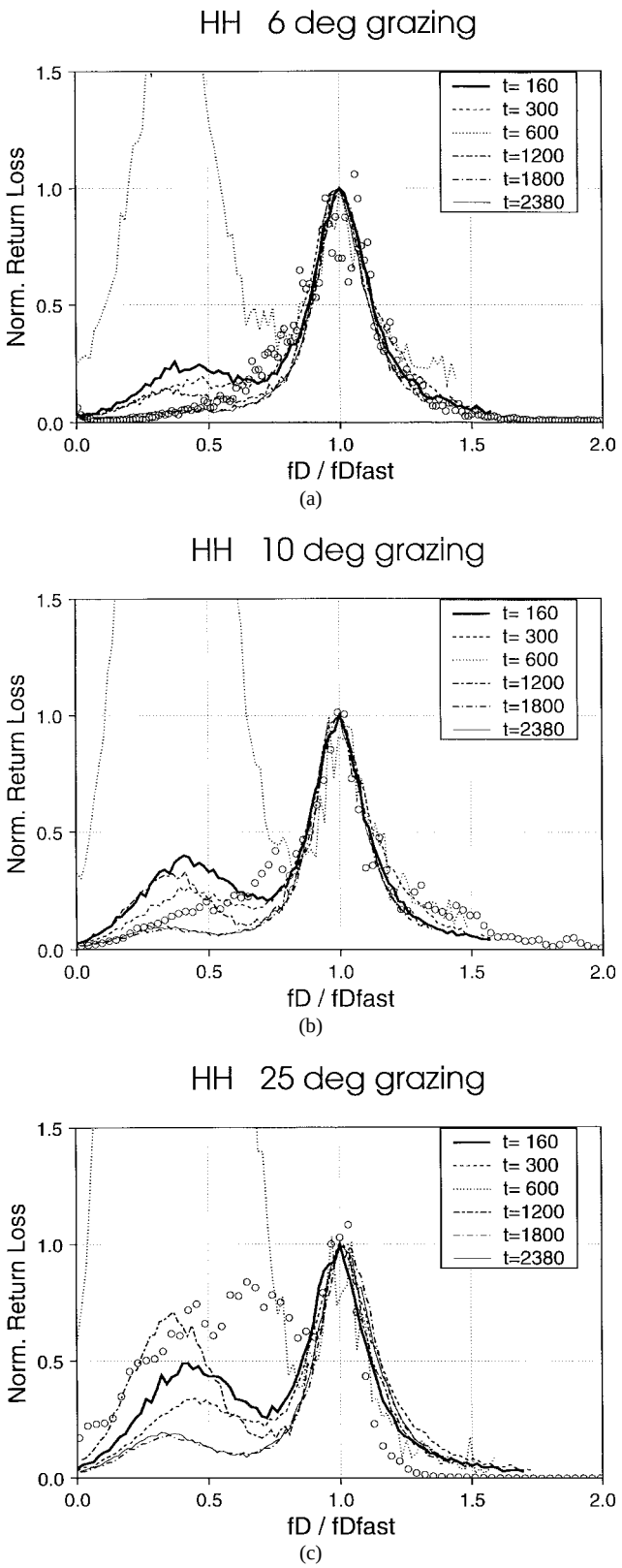

Fig. 11. Simulated normalized HH Doppler spectra as a function of the nondimensional Doppler frequency f_D/f_D^{fast} at various stages of development of the simulated wavefield evolution. Experimental data is plotted as open circles. (a) 6° grazing. (b) 10° grazing. (c) 25° grazing.

are made up of short streaks. These differences become less distinct as the grazing angle is increased, both in the observed and in the simulated RTI's. Time series of returned power

could be simulated by appropriate cuts in the simulated RTI's. It is clear from the low-grazing angle cases that the simulated traces also exhibit the short bursts or spikes observed in time series of field data and that they are much more prominent for HH than for VV pol.

The "peak separation" observed in measured Doppler spectra (i.e., HH having a maximum at a higher frequency than the maximum for VV) is also reproduced by this model for low-grazing angles. As grazing angle increases, the Bragg contribution to the HH Doppler spectrum increase observed in the data is also qualitatively reproduced in the simulations.

It should be stressed that these results have been obtained for a 1-D description of the ocean surface and a very crude model for the description of non-Bragg scattering, where the heuristically determined parameters (cross section per unit area, number of scatterers and their lifetime) have been kept constant as the grazing angle was varied. The description of other observed properties, notably events where σ_{HH} exceeds σ_{VV} and events where σ_{HV} and σ_{VH} differ, would require considering more complex scattering mechanisms.

REFERENCES

[1] J. R. Apel, "An improved model of the ocean surface wave vector spectrum and its effects on radar backscatter," *J. Geophys. Res.*, vol. 99, pp. 16269–16291, 1994.

[2] E. A. Caponi, P. G. Saffman, and H. C. Yuen, "Instability and confined chaos in a nonlinear dispersive wave system," *Phys. Fluids*, vol. 25, pp. 2159–2166, 1982.

[3] E. A. Caponi, "Implementation of TRW's low grazing angle radar return model," TRW Rep. 63817-6004-UT-2.1, Mar. 1996.

[4] D. R. Crawford, P. G. Saffman, and H. C. Yuen, "Evolution of a random inhomogeneous field of nonlinear deep-water gravity waves," *Wave Motion*, vol. 2, pp. 1–16, 1980.

[5] D. B. Creamer, F. Henyey, R. Schult, and J. Wright, "Improved linear representation of ocean surface waves," *J. Fluid Mech.*, vol. 205, pp. 135–161, 1989.

[6] P. A. E. M. Janssen, P. Lionello, and L. Zambresky, "On the interaction of wind and waves," *Phil. Trans. Royal Soc. London*, vol. A329, pp. 289–301, 1989.

[7] A. T. Jessup, W. K. Melville, and W. C. Keller, "Breaking waves affecting microwave backscatter, 1, detection and verification," *J. Geophys. Res.*, vol. 96, pp. 20547–20559, 1991.

[8] A. I. Kalmykov and V. V. Pustovoytenko, "On polarization features of radio signals scattered from the sea surface at small grazingl angle," *J. Geophys. Res.*, vol. 81, pp. 1960–1964, 1976.

[9] V. P. Krasitskii, "Canonical transformation in a theory of weakly nonlinear waves with a nondecay dispersion law," *Sov. Phys.*, vol. JETP71, pp. 921–927, 1990.

[10] ———, "On reduced equations in the Hamiltonian theory of weakly nonlinear surface waves," *J. Fluid Mech.*, vol. 272, pp. 1–20, 1994.

[11] B. M. Lake, H. C. Yuen, H. Rungaldier, and W. E. Ferguson, "Nonlinear deep water waves: Theory and experiment—Part 2: Evolution of a continuous wave train," *J. Fluid Mech.*, vol. 83, pp. 49–74, 1977.

[12] P. H. Y. Lee, J. D. Barter, K. L. Beach, C. L. Hindman, B. M. Lake, H. Rungaldier, J. C. Shelton, A. B. Williams, R. Yee, and H. C. Yuen, "X band microwave backscattering from ocean waves," *J. Geophys. Res.*, vol. 100, pp. 2591–2611, 1995.

[13] P. H. Y. Lee, J. D. Barter, K. L. Beach, E. Caponi, C. L. Hindman, B. M. Lake, H. Rungaldier, and J. C. Shelton, "Power spectral lineshapes of microwave radiation backscattered from sea surfaces at small grazing angles," *Proc. Inst. Elect. Eng.—RSN*, vol. 142, pp. 252–258, 1995.

[14] P. H. Y. Lee, J. D. Barter, K. L. Beach, B. M. Lake, H. Rungaldier, J. C. Shelton, H. R. Thomson Jr., M. D. White, and R. Yee, "TRW experiments at OEL-UC Santa Barbara—Part 1: Pulse-chirped radar calibration and Bragg scattering at small grazing angles," TRW Rep. 63817-6001-UT-6.2, Aug. 1995.

[15] ———, "TRW experiments at OEL-UC Santa Barbara—Part 2: Microwave backscattering from breaking gravity waves," TRW Rep. 63817-6001-UT-7.1, Sept. 1995.

[16] ———, "TRW experiments at OEL-UC Santa Barbara—Part 4: Breaking-wave energy and grazing-angle dependent polarimetric Doppler spectra," TRW Rep. 63817-6001-UT-9.1, Dec. 18, 1995.

[17] P. H. Y. Lee, J. D. Barter, K. L. Beach, E. Caponi, M. Caponi, C. L. Hindman, B. M. Lake, and H. Rungaldier, "Wind-speed dependence of small-grazing-angle microwave backscatter from sea surfaces," *IEEE Trans. Antennas Propagat.*, vol. 44, pp. 333–340, 1996.

[18] P. H. Y. Lee, J. D. Barter, K. L. Beach, B. M. Lake, H. Rungaldier, J. C. Shelton, H. R. Thompson Jr., and R. Yee, "Dependence of polarimetric Doppler spectra on breaking-wave energy," in *Proc. Int. Symp. Geosci. Remote Sensing*, Lincoln, NE, May 1996, vol. IV, pp. 2201–2203.

[19] ———, "Depolarization in microwave scatterometry," in *Proc. Int. Symp. Geosci. Remote Sensing*, Lincoln, NE, May 1996, vol. IV, pp. 2213–2215.

[20] P. H. Y. Lee, J. D. Barter, K. L. Beach, B. M. Lake, H. Rungaldier, J. C. Shelton, H. R. Thomson Jr., M. D. White, and R. Yee, "TRW experiments at OEL-UC Santa Barbara—Part 5: Depolarization in microwave scatterometry," TRW Rep. 63817-6001-UT-10.1, Jan. 1996.

[21] P. H. Y. Lee, J. D. Barter, and H. R. Thomson Jr., "TRW experiments at OEL-UC Santa Barbara—Part 6: Lineshape analysis of breaking-wave Doppler spectra," TRW Rep. 63817-6001-UT-11.1, Jan. 1996.

[22] P. H. Y. Lee, J. D. Barter, K. L. Beach, B. M. Lake, H. Rungaldier, H. R. Thompson Jr., and R. Yee, "Scattering from breaking gravity waves without wind," TRW Rep. 63817-6001-UT-15.4, Mar. 1997.

[23] W. K. Melville, "Wave modulation and breakdown," *J. Fluid Mech.*, vol. 128, pp. 489–506, 1983.

[24] W. J. Pierson Jr. and R. A. Stacy, "The elevation, slope, and curvature spectra of a wind roughened sea surface," NASA Rep. CR-2247, 1973.

[25] S. O. Rice, "Reflection of electromagnetic waves from slightly rough surfaces," *Commun. Pure Appl. Math.*, vol. 4, pp. 351–378, 1951.

[26] M. J. Smith, E. M. Poulter, and J. A. McGregor, "Doppler radar measurements of wave groups and breaking waves," *J. Geophys. Res.*, vol. 101, pp. 14269–14282, 1996.

[27] R. L. Snyder, F. W. Dobson, J. A. Elliot, and R. B. Long, "Array measurements of atmospheric pressure fluctuations above surface gravity waves," *J. Fluid Mech.*, vol. 102, pp. 1–59, 1981.

[28] G. R. Valenzuela, "Theories for the interaction of electromagnetic and oceanic waves—A review," *Boundary Layer Meteorol.*, vol. 13, pp. 61–85, 1978.

[29] G. R. Valenzuela, "Scattering of electromagnetic waves from the ocean," in *Surveillance of Environmental Pollution and Resources by Electromagnetic Waves*, T. Lund, Ed. Norwell, MA: Reidel, 1978, pp. 196–226.

[30] K. D. Ward, C. J. Baker, and S. Watts, "Maritime surveillance radar. Part 1: Radar scattering from the ocean surface," *Inst. Elect. Eng. Radar Signal Processing*, vol. 137, pt. F, pp. 51–62, 1990.

[31] K. D. Ward and P. W. Shepherd, "Bistatic radar sea clutter experiments and spatial coherence," in *Inst. Elect. Eng. Radar 92: Int. Conf.*, Brighton, U.K., 1992, pp. 22–25.

[32] L. B. Wetzel, "On microwave scattering by breaking ocean waves," in *Wave Dynamics and Radio Probing of Ocean Surface*, O. M. Phillips and K. Hasselmann, Eds. New York: Plenum, 1986, pp. 273–284.

[33] H. C. Yuen and B. M. Lake, "Nonlinear dynamics of deep-water gravity waves," *Adv. Appl. Mech.*, vol. 22, pp. 67–229, 1982.

[34] V. E. Zakharov, "Stability of periodic waves of finite amplitude on the surface of a deep fluid," *Zh. Prikl. Mekh. Tekh. Fiz.*, vol. 65, pp. 86–94, 1968; transl. *J. Appl. Mech. Tech. Phys.*, vol. 2, pp. 190–194, 1968.

Enrique A. Caponi did his undergraduate work in physics at the Facultad de Ciencias Exactas, Universidad Nacional de Buenos Aires, Argentina, and received the Ph.D. degree in physics from the University of Maryland in 1974.

He joined the Laboratorio de Hidraulica Aplicada, Ezeiza, Argentina, in 1975, intending to set up a research program for the study of the River Plate estuary. In 1976 he was Visiting Professor at the Instituto de Fisica, Universidade Federal do Rio Grande do Sul, Porto Alegre, Brazil, where he taught a graduate course and was involved in research in plasma physics. He joined TRW, Redondo Beach, CA, in 1978. Since then, he has participated in the U.S. Navy, Defense Advanced Research Projects Agency, Office of Naval Research, and Office of the Secretary of Defense funded projects, as well as various international research and development projects. Under these programs, he has conducted research in ocean surface and subsurface physics and their relevance to nonacoustic anti-submarine warfare and ocean remote sensing and detection and has been responsible for the design and development of a substantial number of the computer codes in use by the Ocean Technology Department, TRW. He has published numerous reports and refereed papers.

Bruce M. Lake received the B.S.E. (Hon.) degree from Princeton University, Princeton, NJ, in 1963, and the M.S. and Ph.D. degrees in aeronautics (fluid mechanics) from the California Institute of Technology, Pasadena, in 1964 and 1969, respectively.

He joined the Advanced Instrumentation Department of TRW Defense and Space Systems Group in 1969. In 1973 he became Head of the Experimental Hydrodynamics Section of the Fluid Mechanics Department of TRW. He became Assistant Manager of the department in 1977 and Manager in 1981. In 1996 he became Manager of the Computational Physics Business Area of TRW while continuing to manage TRW's activities in the U.S./U.K. nonacoustic anti-submarine warfare program sponsored by Office of the Secretary of Defense. He has published extensively, including contributions to books and review articles. His 30 years experience in experimental fluid mechanics and the application of instrumentation and sensors to geophysical investigations includes work in nonlinear wave dynamics, wave instabilities, wave-current interactions, radar scattering from ocean waves, as well as planning of field experiments and design of deployable sensor packages.

Dr. Lake is a member of the National Academy of Engineering and a TRW Technical Fellow and has served on committees for the National Academy of Science.

Henry C. Yuen received the B.A. (Hon.) and B.S. (Hon.) degrees in mathematics from the University of Wisconsin, Madison, in 1969, and the Ph.D. degree in applied mathematics (fluid mechanics) from the California Institute of Technology, Pasadena, in 1973.

He joined TRW's Department of Fluid Mechanics in 1974 where he produced some seminal work in nonlinear wave dynamics. He was principal investigator and team leader for nearly ten years in the surface hydrodynamics research and modeling effort under the Navy-SSBN Security Program, working in almost every aspect of surface and subsurface hydrodynamics relevant to nonacoustic submarine detection. He has been Team Leader and Principal Investigator in Defense Advanced Research Projects Agency and Office of Naval Research projects involving model prediction, data interpretation and construction of an end-to-end simulation model for multisensor remote detection. He has over 70 publications in refereed journals and over 40 classified and unclassified TRW technical reports. He has been a Technical Fellow at TRW, a Visiting Lecturer at the Enrico Fermi International School of Physics in Ocean Physics, Italy, an Invited Speaker at numerous universities and conferences, and has also acted as a reviewer for the National Science Foundation, National Research Council, and the Army Research Center.